

# Epitaxial Growth of Aurivillius $\text{Bi}_3\text{Fe}_2\text{Mn}_2\text{O}_x$ Supercell Thin Films on Silicon

James P. Barnard, Robynne L. Paldi, Matias Kalaswad, Zihao He, Hongyi Dou, Yizhi Zhang, Jianan Shen, Dongqi Zheng, Neil R. Dilley, Raktim Sarma, Aleem M. Siddiqui, Peide D. Ye, and Haiyan Wang\*



Cite This: *Cryst. Growth Des.* 2023, 23, 2248–2256



Read Online

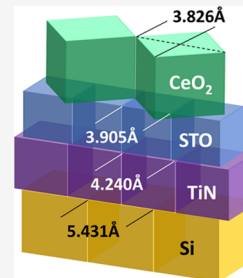
ACCESS |

Metrics & More

Article Recommendations

Supporting Information

**ABSTRACT:** Nanoelectronic devices integrated with functional complex oxides have drawn much attention in recent years. However, due to material and processing compatibility issues, integrating functional complex oxides with Si-based devices is challenging, and success has been limited. As an example, the  $\text{Bi}_3\text{Fe}_2\text{Mn}_2\text{O}_x$  (BFMO) supercell system, a single-phase layered oxide made by compositing  $\text{BiFeO}_3$  and  $\text{BiMnO}_3$ , has been studied for much of the past decade for its unusual layered Aurivillius structure and magnetic and ferroelectric properties. However, most of the BFMO thin film growth has been demonstrated on single-crystal oxide substrates such as  $\text{SrTiO}_3$  and  $\text{LaAlO}_3$ . In this work, we demonstrate that the BFMO layered supercell phase can be integrated on Si with high epitaxial quality using a buffer stack of TiN/ $\text{SrTiO}_3$ / $\text{CeO}_2$ . Further understanding of the strain-controlled growth of the BFMO supercell phase has allowed such Si integration. Microstructure, magnetic, ferroelectric, and optical properties of the BFMO films on Si have been characterized and compared with those of BFMO on  $\text{SrTiO}_3$  single-crystal substrates, demonstrating comparable epitaxial quality and physical properties. Integrating multiferroic BFMO oxides on Si demonstrates the potential of layered supercell oxides in practical device applications such as ferroelectric field effect transistors.



## INTRODUCTION

Functional complex oxides with unique functionalities have drawn much attention in recent years in the development of nanoelectronic devices.<sup>1–3</sup> Multiferroic oxide materials, those possessing multiple ferroic orders, e.g., exhibiting simultaneous ferromagnetism and ferroelectricity, have been an area of research for many decades.<sup>4–7</sup> The particular interest in these materials stems from their use in memory storage, such as spintronic tunnel junction devices,<sup>8</sup> magnetoelectric random access memory,<sup>9,10</sup> four-state memory,<sup>11</sup> and spin filters.<sup>12</sup>

Among the known single-phase multiferroic materials, the  $\text{BiFeO}_3$  (BFO) and  $\text{BiMnO}_3$  (BMO) perovskite oxides are well explored systems. The BFO system presents ferroelectric properties with a high Curie temperature of 1103 K and weak antiferromagnetic properties, with a Néel temperature of 640 K.<sup>13</sup> The BMO system, conversely, displays strong ferromagnetic properties with a Curie temperature of 105 K but lacks robust ferroelectricity, with a Curie temperature of 760 K.<sup>13</sup> The fact that these systems do not present simultaneous ferroelectric and magnetic properties is due to the converse physical requirements for the two orders. Namely, ferroelectricity typically requires empty d-orbitals, while ferromagnetism is produced by partially filled d-orbitals.<sup>14</sup> However, this contradicting requirement can be satisfied in nanocomposites by forming a segregated material using two immiscible phases.<sup>15</sup>

Since the time that the theoretically predicted single-phase multiferroic system of  $\text{BiFeMnO}$  (BFMO) with ordered Fe

and Mn ions was proposed, multiple experimental demonstrations have been performed.<sup>13,16–21</sup> Choi *et al.* attempted the growth of the nanochckerboard structure, resulting in the  $\text{BiFe}_{0.5}\text{Mn}_{0.5}\text{O}_3$  tetragonal phase.<sup>20</sup> This phase was strongly ferromagnetic but lacked ferroelectricity.<sup>20</sup> Chen *et al.* discovered the proposed multiferroic  $\text{Bi}_3\text{Fe}_2\text{Mn}_2\text{O}_x$  (BFMO322) supercell (SC) phase with a superlattice structure on  $\text{LaAlO}_3$  (LAO) substrates ( $a = 3.793 \text{ \AA}$ ) via substrate strain.<sup>22,23</sup> This new layered oxide is an Aurivillius phase, where  $\text{Bi}_2\text{O}_3$  layers separate out from the other cation layers, in this case  $\text{FeO}_6/\text{MnO}_6$  octahedra.<sup>24,25</sup>

Following this discovery of the SC phase, Zhu *et al.* examined the role of strain in the SC growth, confirming that misfit strain was a vital factor.<sup>26</sup> Li *et al.* further revealed that a thin buffer layer of  $\text{CeO}_2$  could be used to generate sufficient strain to promote growth of the desired SC phase on both  $\text{SrTiO}_3$  (STO) and LAO substrates.<sup>25</sup> It is noted that previous reported studies on the BFMO322 SC have been performed mostly on single-crystal oxide substrates, such as STO and LAO substrates.<sup>27–29</sup> Due to material and processing compatibility issues, integrating these functional complex

Received: November 8, 2022

Revised: February 24, 2023

Published: March 9, 2023



ACS Publications

© 2023 American Chemical Society

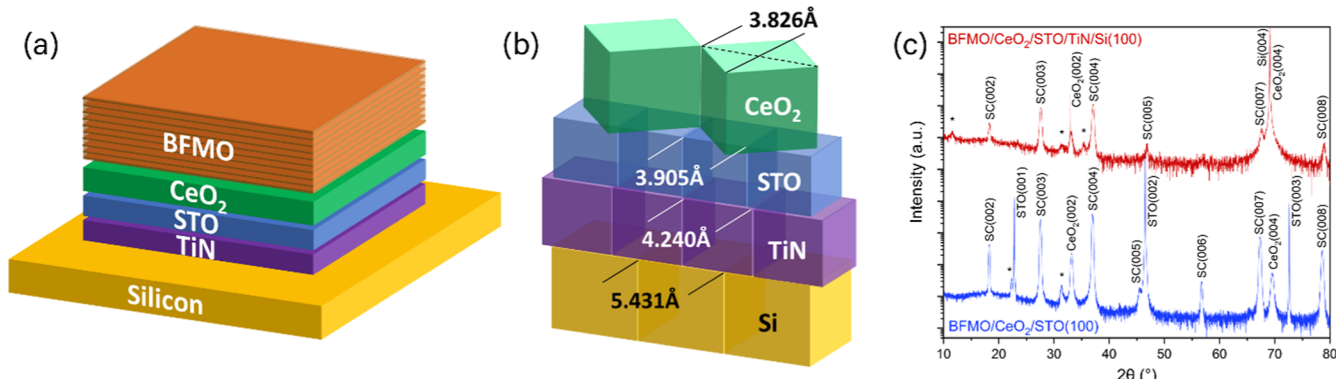


**Figure 1.** Film structure shown in (a) layer stack used to grow the film, (b) lattice matching between each layer, and (c) XRD  $\theta$ - $2\theta$  scan of the film on STO and Si substrates.

oxides with Si-based devices is challenging, and very limited success has been achieved.<sup>30</sup> On the other hand, practical device applications and cost effectiveness for fabrication mean that the integration of these new multiferroic oxides on Si is of great technological importance.<sup>31</sup>

In this work, we propose to integrate the multiferroic BFMO SC structure on Si for its potential as the ferroelectric layer for ferroelectric field effect transistors (FeFETs) and the ferromagnetic layer for magnetic memory devices. One of the major challenges for oxide–Si integration is the large lattice mismatch between Si and the oxide, as Si has a lattice parameter of 5.431 Å,<sup>31</sup> which is significantly larger than that of common single-crystal oxide substrates (e.g.,  $a_{\text{STO}} = 3.905$  Å).<sup>32</sup> Since BFMO with a buffer layer of CeO<sub>2</sub> is known to grow on STO, it could be ideal to grow STO directly on Si before depositing the BFMO/CeO<sub>2</sub> layer stack. The lattice parameters appear to have reasonable matching with a 45° in-plane rotation between Si and STO (i.e.,  $\sqrt{2}a_{\text{STO}} = 5.523$  Å,  $a_{\text{Si}} = 5.431$  Å). However, there are challenges with this approach. First, STO has been reported to demonstrate mixed orientation matching on Si, rather than the preferred orientation growth needed for high-quality films.<sup>33,34</sup> Second, the etched Si surface could rapidly oxidize under the oxygen atmosphere required to grow high-quality oxides such as STO. To address these challenges, a unique buffer layer stack of TiN/SrTiO<sub>3</sub>/CeO<sub>2</sub> has been proposed to integrate the BFMO SC phase on Si and to effectively mitigate the large mismatch, as shown in Figure 1a. TiN is selected here to reduce the lattice mismatch from Si, considering the unique domain matching epitaxy of 4:3 between TiN(200) and Si(400), and to prevent oxidation of the Si surface as it can be grown under vacuum conditions.<sup>30,31,35</sup> A further reduction of the lattice parameter is accomplished by STO. Finally, CeO<sub>2</sub> is selected to establish the SC growth on STO as previously demonstrated.<sup>22</sup> While CeO<sub>2</sub> has a significantly larger lattice parameter ( $a = 5.411$  Å), the 45° in-plane rotation (see Figure S1 for the XRD Phi scan) leads to a similar effective lattice parameter ( $a/\sqrt{2} = 3.826$  Å) to STO, as illustrated in Figure 1b. In this study, the microstructure, magnetic, ferroelectric, and optical properties of the BFMO films on Si are characterized and compared with those of the BFMO on STO single-crystal substrates. This work could pave the way for other Aurivillius phases to be integrated onto Si utilizing this buffer layer technique.

## EXPERIMENTAL SECTION

**Thin Film Growth.** Pulsed laser deposition (PLD) was used to deposit the epitaxial BFMO films and the buffer layers onto LaAlO<sub>3</sub>(001), SrTiO<sub>3</sub>(001), and Si(001) single-crystal substrates. The BFMO target was created by pressing a mixture of the Bi<sub>2</sub>O<sub>3</sub>, MnO<sub>2</sub>, and Fe<sub>2</sub>O<sub>3</sub> powders and sintering at 800 °C for 3 h. The Si substrates were etched prior to deposition using hydrofluoric acid (HF) to remove the SiO<sub>2</sub> native oxide. A KrF excimer laser ( $\lambda = 248$  nm) was used in the PLD process with an incidence angle of 45°. Growths of the TiN, SrTiO<sub>3</sub>, and CeO<sub>2</sub> buffer layers were performed sequentially before the BFMO deposition. The target substrate distance was held constant at 4.5 cm for all depositions. The specific growth parameters are shown in Table S1. Following the deposition, all samples were annealed in 200 Torr O<sub>2</sub> during cooling (10 °C·min<sup>-1</sup>).

**Microstructure Characterization.** The films were examined using X-ray diffraction (XRD, PANalytical Empyrean) and transmission electron microscopy (TEM) and scanning TEM (STEM) combined with energy-dispersive X-ray spectroscopy (EDS) mapping, all conducted using the Thermo Fisher TALOS F200X. TEM samples were prepared by the conventional grinding–dimpling method and precision ion milling polishing using the Gatan PIPS 695.

**Property Characterization.** The magnetic properties of the samples were measured using the Quantum Design MPMS-3 SQUID magnetometer in the VSM mode. The magnetic field was applied in the in-plane and out-of-plane directions. Ferroelectric hysteresis loops ( $P$ – $E$ ) were analyzed using the Radian Technologies Precision LC II ferroelectric tester. The magnetoelectric coupling coefficient was measured using the Radian Technologies magnetoelectric bundle. The piezoelectric force microscopy (PFM) measurements were completed using a Bruker Dimension Icon with SCM-PIT probes. The optical properties of the films were measured with a J.A. Woollam RC2 spectroscopic ellipsometer. The psi and delta data was first fit to the B-spline model before constructing an oscillator using the Lorentz model. The mean square error (MSE) was less than 5 for all models.

**Device Fabrication.** Atomic layer deposition (ALD) was used to deposit 4 nm of Al<sub>2</sub>O<sub>3</sub> at 175 °C using (CH<sub>3</sub>)<sub>3</sub>Al (TMA) and H<sub>2</sub>O as Al and O precursors and to deposit 2.5 nm of In<sub>2</sub>O<sub>3</sub> at 225 °C with (CH<sub>3</sub>)<sub>3</sub>In (TMIn) and H<sub>2</sub>O as Al and O precursors. Thickness was confirmed by ellipsometry (Gaertner L116A), TEM, and atomic force microscopy. The TMIn precursor was heated to 60 °C to provide sufficient vapor pressure, and N<sub>2</sub> with a flow rate of 40 sccm was used as the carrier gas. In<sub>2</sub>O<sub>3</sub> channel isolation was done by plasma dry etching (BCl<sub>3</sub>; 15 sccm, Ar: 60 sccm; pressure: 0.6 Pa, RF source power: 100 W; RF bias power: 50 W; time: 30 s). E-beam evaporation was used to deposit 60 nm of Ni as source/drain contacts, patterned by direct write laser lithography. Annealing under O<sub>2</sub> was carried out at 300 °C (RTA furnace).

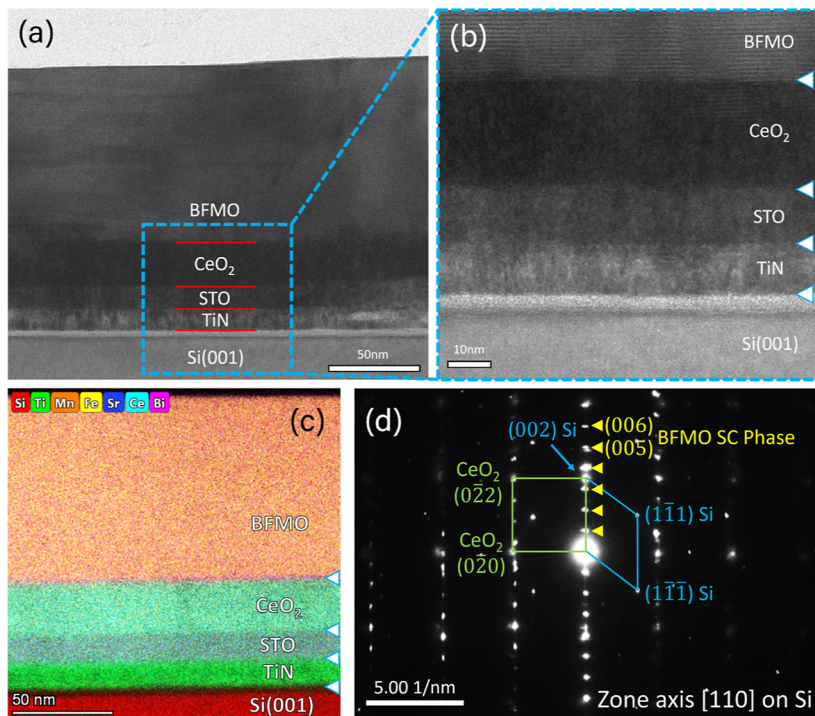


**Figure 2.** Microstructural characterization through TEM. (a) HR-TEM image of the layer stack on the Si substrate. (b) Higher magnification showing atomic-level epitaxy between layers. (c) EDS results confirming the composition of each layer. (d) SAED pattern showing epitaxial growth quality with expected orientation between layers.

## ■ RESULTS AND DISCUSSION

To better evaluate the growth of BFMO on Si using the proposed buffer layer stack, LAO and STO substrate samples were deposited as references. The BFMO SC phase is known to grow on both LAO and STO substrates when a buffer layer of CeO<sub>2</sub> is utilized.<sup>25</sup> XRD analysis was first performed to evaluate the crystalline quality of the films. Figure 1c shows the results for the BFMO films grown on the Si and STO substrates, confirming obvious SC peaks, marked as SC (00l), and high-quality crystal growth on both substrates. Several minor peaks marked with the “\*” symbol were considered unidentified phases. Figure S2 in the Supporting Information contains the XRD data for the growth on the LAO substrate, showing comparable results to those on STO. The BFMO SC phase is reported to grow well under compressive strain.<sup>26</sup> The BFMO peaks on Si have shifted up by 0.3° for peaks with higher indices, indicating a lower compressive strain in the Si-based sample compared to that in the samples grown on single crystalline oxide substrates.<sup>22</sup> This can be explained by the fact that the STO grown on TiN will be under tensile strain due to the smaller lattice parameter of STO. This peak shift indicates that the STO is unable to fully relax this tensile strain, and it has passed on to the subsequent layers, resulting in less compressive strain in the BFMO film on Si. It is calculated that the difference in strain between the two BFMO films is 0.2%. The film quality of the BFMO film on the Si substrate, identified by the sharpness and intensity of the XRD peaks, is comparable to that of the samples using STO and LAO substrates, confirming that the buffer layer stack was successful in initiating the SC growth on Si.

Further characterization of the epitaxial quality of the BFMO SC on Si was performed by TEM. It was found that the films had grown uniformly in the layered SC structure, as shown in Figure 2a. The high-resolution TEM image shown in

Figure 2b confirms the expected phase and epitaxial growth of each buffer layer as labeled. The BFMO was identified as the expected Aurivillius phase, easily recognized by the clear layered structure. Although the contrast varies across the film, the epitaxial quality of the phase is excellent throughout the film thickness, as confirmed by the cross-section TEM image over the entire film thickness (~95 nm) shown in Figure S3. The variation in contrast is due to minor differences in foil thickness of the TEM sample. EDS confirms sharp interfaces between each buffer layer and the BFMO film without any obvious diffusion between layers as seen in Figure 2c. The selected area electron diffraction (SAED) pattern shown in Figure 2d contains the distinctive satellite diffraction patterns confirming that the SC layered structure is the primary phase of BFMO present in the sample. While these images are limited in resolution by the TEM used to image the sample, previous work of high-resolution STEM analysis has been conducted on the BFMO SC structure using an aberration-corrected instrument.<sup>22</sup>

Considering the multiferroic nature of the BFMO films, magnetic hysteresis ( $M-H$ ) measurements were first conducted by measuring the magnetization ( $M$ ) of the films by sweeping the applied magnetic field ( $H$ ). Both in-plane and out-of-plane field conditions were measured to explore any easy axis (anisotropic) effects rising from the layered structure of the film.

The  $M-H$  loops of the BFMO SC are shown in Figure 3. A clear hysteresis is present with strong saturation and remanence, indicating the presence of a magnetic order. Previous work on the BFMO SC phase, including the use of density functional theory to understand the material's behavior, has concluded that the magnetic order present in this phase is ferrimagnetism.<sup>22,25,27,29</sup> In this unique layered structure, the Mn and Fe cations are arranged in a zigzag-

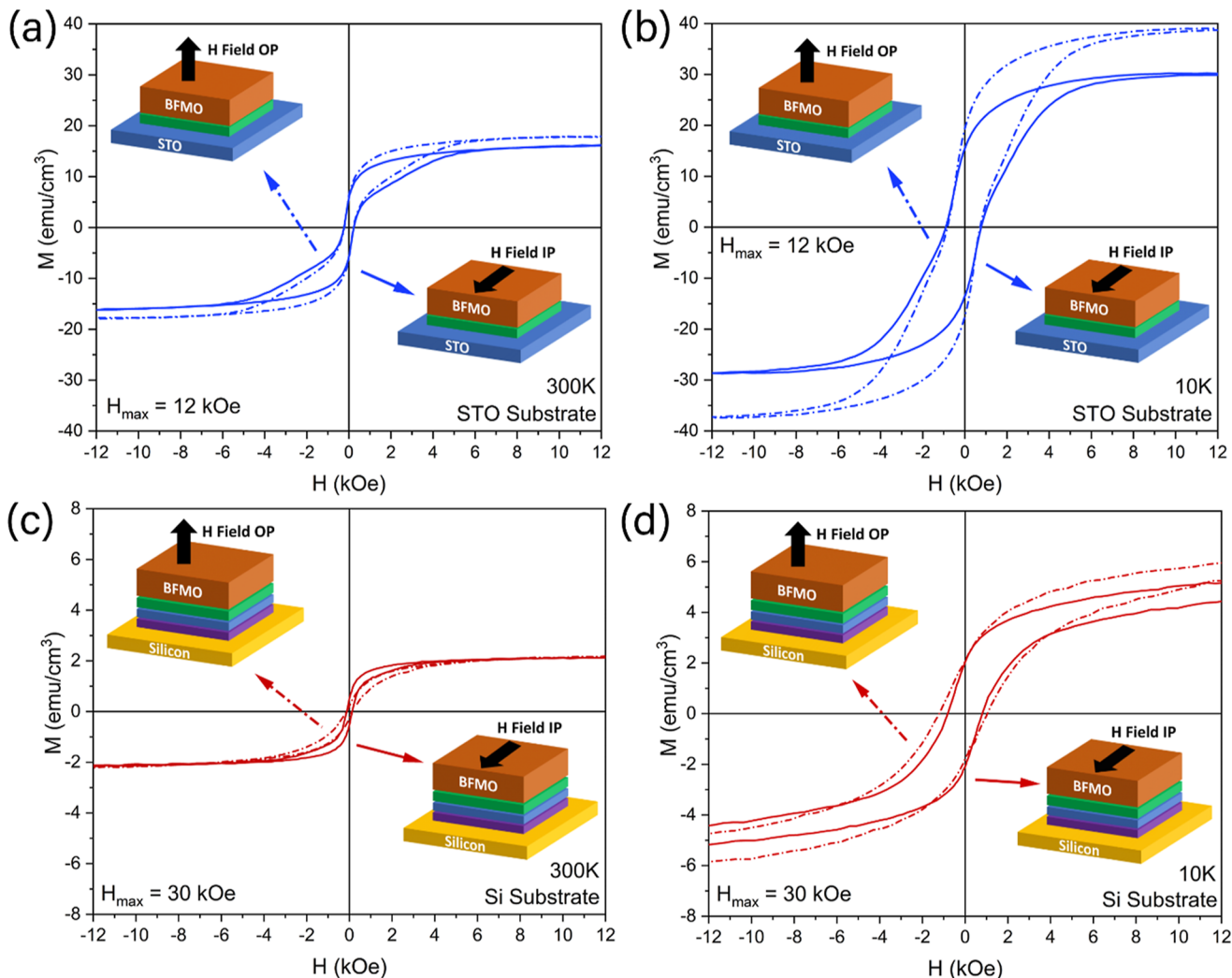


**Figure 3.** Magnetic characterization of the BFMO SC film on STO and Si substrates at temperatures of (a,c) 300 and (b,d) 10 K. The plotted field range is selected to highlight coercivity and remanence, while the actual maximum applied field to ensure saturation is listed in each case.

shaped pattern, which is thought to give rise to a spin canting effect.<sup>22</sup> There is also a lower crystal symmetry in the phase, possibly resulting in the anisotropic magnetic properties observed in the STO-based sample.<sup>22</sup> It is noted that the large difference between the two sample orientations shown in Figure 3b is likely due to sample mounting changes and is within our measurement reproducibility error for these samples. While the coercivity of the two samples is similar, the remanence and saturation magnetization are significantly reduced in the Si-based sample. A possible explanation for the difference between the STO- and Si-based samples is the different strain states for the two cases, as calculated and discussed in the XRD section. STO single-crystal samples have a more rigid substrate for BFMO growth and thus a higher compressive strain for the BFMO film.<sup>22</sup>

It is also noted that the coercivity and saturation magnetization increase at lower temperature, a possible indication of a transition in one of the magnetic orders. An additional study of the dependence of magnetization on temperature was performed, yielding a weak transition at 32 K, as shown in Figure S4. The small magnitude of this transition indicates that a decrease in thermal action at low temperature is primarily responsible for the increased saturation magnetization.

The ferroelectric order in this phase is generated by the Bi atoms and the biaxial compressive strain in the out-of-plane direction, leading to a weak polarization axis.<sup>27</sup> In order to characterize the ferroelectric properties of the BFMO film, polarization–field (*P*–*E*) hysteresis measurements were performed. The results are shown in Figure 4a,c. The BFMO films on STO and Si show relatively weak polarization magnitude and some leakage. Such weak polarization properties are attributed to multiple causes. First, a high density of point defects in oxides could lead to the leakage and weak polarization in ferroelectric oxide thin films.<sup>36–38</sup> Approaches such as post-deposition oxygen annealing along with tuned growth temperature and pressure conditions could minimize point defects and thus improve the overall switching properties.<sup>39,40</sup> Second, it has been discovered that Aurivillius phases tend to exhibit stronger polarization along the in-plane direction.<sup>41</sup> Thus, improving the growth and texture could also improve the overall properties. Our efforts focused on reducing the oxygen vacancy and grain boundary density and improving film epitaxial quality are currently ongoing. Some of the initial successes are shown in this section. Third, the BFMO films in this work are relatively thin (~95 nm), while thicker films tend to have improved polarization properties. However, the strain-controlled BFMO SC phase cannot grow beyond 100 nm,

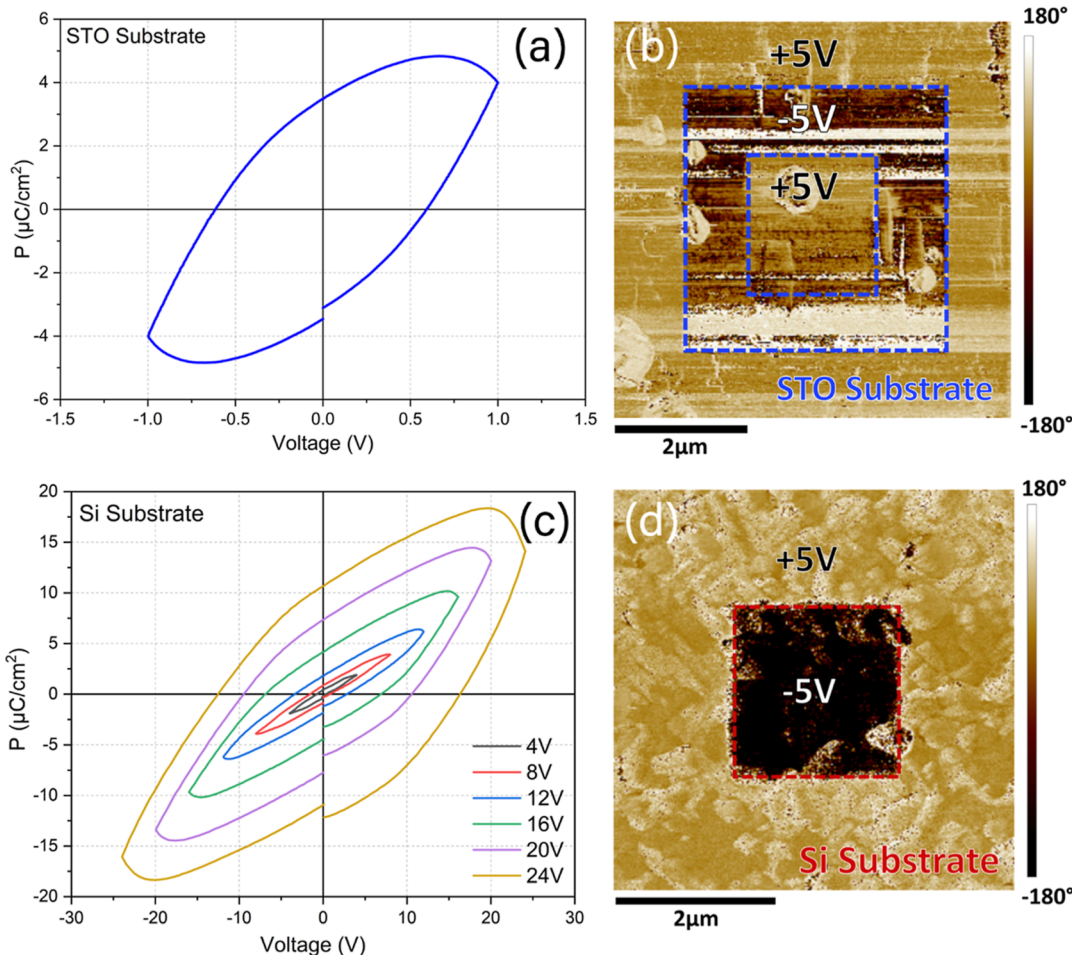


**Figure 4.** Electrical characterization of the BFMO SC film on (a,b) STO and (c,d) Si substrates. (a,c)  $P-E$  hysteresis loops allow for basic characterization of the ferroelectric properties of the film. (b,d) PFM phase maps show the ability of the film to hold the orientation of the polarization in a 2D area.

where a pseudo-cubic phase becomes preferred.<sup>22</sup> The study of the growth of thicker BFMO SC films is currently ongoing in the laboratory.

Further characterization was performed using PFM to probe the surface with an AC signal superimposed on a DC bias. The DC bias is used to “write” the polarization of the surface, while the AC signal can be used to “read” the polarization. After a pattern was written on the surface, the remnant surface polarization could be measured to determine the ferroelectric properties of the material. The polarization phase results are shown in Figure 4b,d, suggesting a switchable ferroelectric domain structure for both the STO and Si samples. The PFM magnitude data corresponding to this phase data is shown in Figure S5; however, the magnitude is small, as discussed. Additional LAO substrate data can be found in Figure S6.

Additional measurements were performed on a single surface point in PFM to demonstrate the switching behavior of the material and a computed  $d_{33}$  piezoelectric coefficient, provided in Figure S7. Although the ferroelectric polarization is weak, the results of the measurements indicate that the switching properties of the film grown on Si are slightly stronger than those of the film grown on STO. A possible explanation is again related to the strain difference between the two samples due to the buffer layers. Ferroelectric polarization arises from the asymmetric strain, so it can be concluded that a

larger misfit strain in the Si sample could lead to a stronger polarization magnitude.<sup>27</sup>

The magnetoelectric coupling property of BFMO was also explored. Linear magnetoelectric coupling was present in the sample, shown in Figure S8, with a comparable magnitude to other recently explored materials.<sup>30,42</sup> While the magnetoelectric coupling effect in Bi-based nanocomposite thin films is often attributed to the magnetoelastic and piezoelectric properties, where strain can interact with the ferroic orders and become the coupling mechanism, this cannot explain the coupling in the single-phase BFMO films.<sup>43,44</sup> The exact coupling mechanism is currently unknown. However, this coupling has particular applications in the memory storage field, such as in magnetoelectric random access memory, where an electric field, which is significantly more power-efficient, can be used to set a magnetic state or where multiple data bits can be saved simultaneously by utilizing both orders.<sup>9,10</sup>

The optical properties of the BFMO SC were explored using spectroscopic ellipsometry, which measures the amplitude ratio ( $\Psi$ ) and phase difference ( $\Delta$ ) of the in-plane and out-of-plane polarization components of the reflection.<sup>45</sup> The raw optical data values can be found in Figure S9. The data measured from the samples was then used to fit the dielectric function of the BFMO film using a Lorentz oscillator model. This model was designed to only show the contributions of the BFMO film. In order to do this, samples consisting of only the buffer layers on

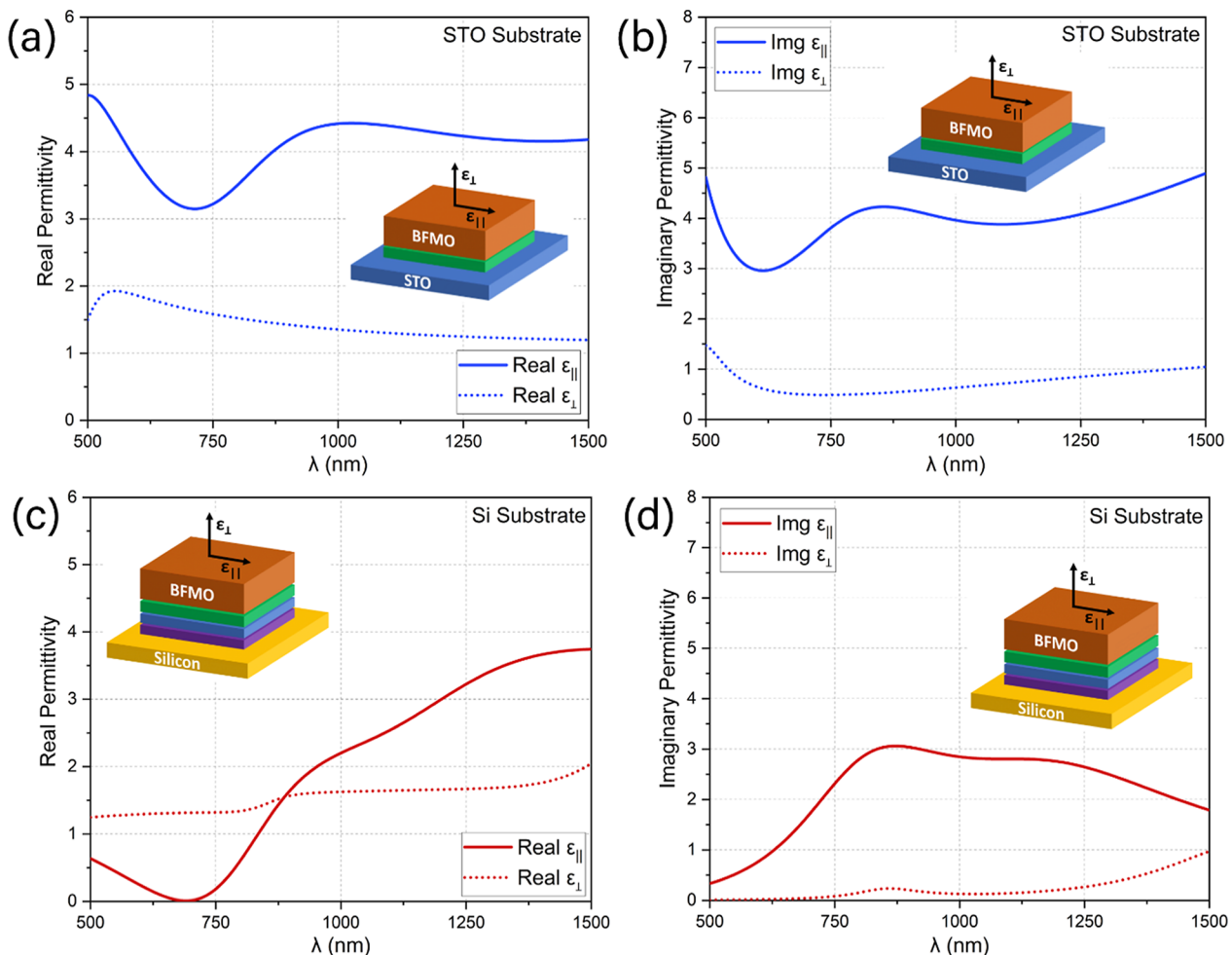


**Figure 5.** Optical characterization of the BFMO SC films. The (a) real and (b) imaginary permittivity for the film on the STO substrate. The (c) real and (d) imaginary permittivity for the film on the Si substrate.

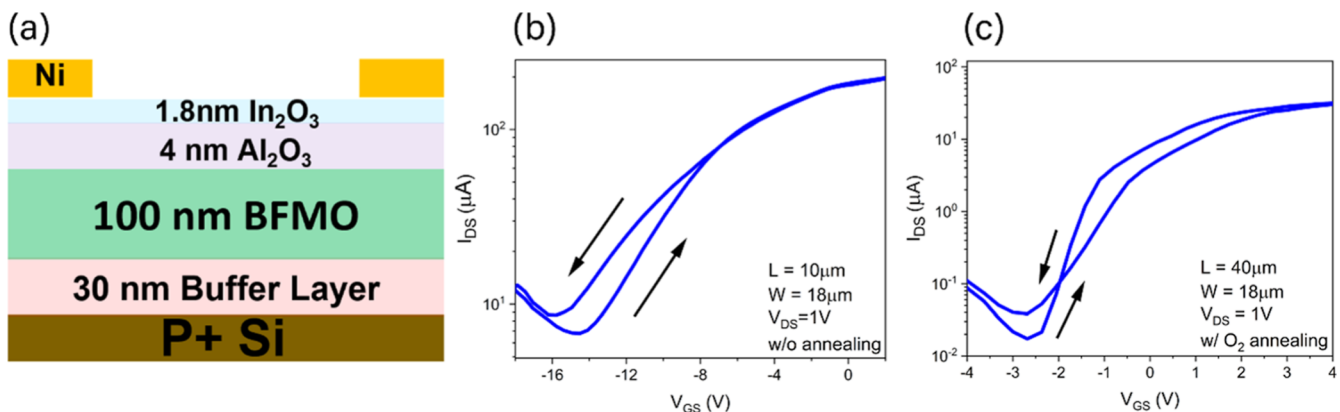


**Figure 6.** Device testing of the FeFET. The (a) schematic and the output transfer characteristics (b) before and (c) after O<sub>2</sub> annealing.

each substrate were deposited, and a series of models were fit to the buffer layer optical properties. The saved models were then used in the complete model of the full BFMO sample to effectively remove the contributions of the substrate and buffer layers from the data. Finally, an additional model was fit to only the BFMO film and was used to generate the data. The dielectric constants (i.e., permittivity,  $\epsilon_{\parallel}$  and  $\epsilon_{\perp}$ ) are shown in Figure 5. The BFMO on both substrates is highly anisotropic, which is expected considering the anisotropic structure of the

layered oxide. These types of responses are typically found in highly anisotropic nanocomposite structures such as vertically aligned nanocomposites (VANs), where two dissimilar phases are integrated as composite materials. Thus, it is notable to find such highly anisotropic optical properties in a single-phase SC structure.<sup>46–48</sup> Although the model has been adjusted to remove contributions from buffer layers, there are still some differences between the dielectric properties of the STO and Si samples. These differences could be attributed to the varying

film quality between the STO and Si samples and errors introduced by the complex fitting process. However, the main features (e.g., peak positions, overall trends) of both curves indicate that the two samples have very similar optical responses.

A FeFET was fabricated to show the possibility of device applications with the BFMO SC integrated on Si. FeFET devices have become an area of interest in recent years due to the possibility of in-memory computing—a game changer for neural networking applications.<sup>49</sup> The BFMO demonstrates excellent compatibility with the state-of-the-art ultrathin ALD semiconductor In<sub>2</sub>O<sub>3</sub> at the device level. A FeFET based on BFMO is realized with the device schematic shown in Figure 6a and fabricated with a thermal budget below 300 °C. A counterclockwise loop is clearly observed in Figure 6b, which proves the ferroelectric control induced by the BFMO layer. The on–off ratio is further improved by annealing the transistor under O<sub>2</sub> for 1 min to reduce the carrier density of the In<sub>2</sub>O<sub>3</sub> film, as shown in Figure 6c. It is notable that the transfer output curve of the annealed device illustrates a minor counterclockwise loop, which is contributed to by both interface traps and ferroelectric polarization. Current results indicate that BFMO is a promising candidate for next-generation ferroelectric memory transistors, especially in back-end-of-line applications. For an additional discussion on the FeFET switching mechanism and partial switching states, see the explanation in the Supporting Information and Figure S10.

This work contains the first successful attempt to grow the BFMO SC on silicon. The BFMO SC has not been used in device fabrication in previous work. This demonstration of FeFET devices using the BFMO SC on Si opens potential for other layered multiferroic oxides, e.g., BiAlMnO<sup>50–52</sup> and BiMoMnO<sup>53</sup> in practical device applications. Future work on integrating these new layered oxides and other multiferroic oxides on Si will be necessary for such device demonstrations. Challenges remain in the area of simplifying the buffer stack structures required for the oxide–Si integration toward practical device fabrication and preparing ultra-thin multiferroic layered oxides<sup>54</sup> toward low-power switching FeFET devices. Ultra-thin film deposition presents unique challenges for most of the perovskite oxides. Interestingly, layered Aurivillius phases present novel opportunity in achieving ultra-thin layer growth using techniques such as reflection high-energy electron diffraction, which has been used to identify the growth of individual layers in the Aurivillius structure,<sup>55</sup> in this case Bi<sub>2</sub>O<sub>2</sub> and MnO<sub>6</sub>/FeO<sub>6</sub>.

## CONCLUSIONS

The BFMO SC phase has been epitaxially grown on silicon in this work utilizing a unique buffer layer stack of TiN/SrTiO<sub>3</sub>/CeO<sub>2</sub> to optimize the strain in the BFMO film, mitigate the large lattice mismatch, and promote the growth of the layered Aurivillius phase. The BFMO SC on Si retains the unique layered structure and physical properties comparable to those observed with STO and LAO substrates. This phase has been shown to demonstrate strong optical anisotropy by ellipsometry measurements. The preliminary FeFET device demonstration using the BFMO SC integrated on Si presents the potential of multiferroic layered oxides for future FeFET devices, spintronics, and memory devices. The growth of this new BFMO layered SC phase on Si demonstrates the power of strain-controlled growth using the buffer layer approach, which

can also be applied to other functional complex oxide systems for Si-based devices.

## ASSOCIATED CONTENT

### Supporting Information

The Supporting Information is available free of charge at <https://pubs.acs.org/doi/10.1021/acs.cgd.2c01300>.

XRD Phi scan showing 45° in-plane rotation of CeO<sub>2</sub> on STO; detailed PLD growth parameters of each film discussed; structural (XRD) and electrical property (PFM) characterization of the reference sample on the LAO substrate; polarization amplitude map for STO and Si samples; temperature-dependent magnetism study and magnetoelectric coupling of the sample on the STO substrate; electrical phase–amplitude switching measurement of the sample on the Si substrate; ellipsometry raw optical data used to obtain the dielectric function; and additional diagram and discussion on FeFET switching states ([PDF](#))

## AUTHOR INFORMATION

### Corresponding Author

Haiyan Wang – School of Materials Engineering, Purdue University, West Lafayette, Indiana 47907, United States; School of Electrical and Computer Engineering, Purdue University, West Lafayette, Indiana 47907, United States;  [orcid.org/0000-0002-7397-1209](https://orcid.org/0000-0002-7397-1209); Email: [hwang@purdue.edu](mailto:hwang@purdue.edu)

### Authors

James P. Barnard – School of Materials Engineering, Purdue University, West Lafayette, Indiana 47907, United States;  [orcid.org/0000-0002-7570-952X](https://orcid.org/0000-0002-7570-952X)

Robynne L. Paldi – Sandia National Laboratories, Albuquerque, New Mexico 87185, United States

Matias Kalaswad – Sandia National Laboratories, Albuquerque, New Mexico 87185, United States

Zihao He – School of Electrical and Computer Engineering, Purdue University, West Lafayette, Indiana 47907, United States

Hongyi Dou – School of Materials Engineering, Purdue University, West Lafayette, Indiana 47907, United States

Yizhi Zhang – School of Materials Engineering, Purdue University, West Lafayette, Indiana 47907, United States

Jianan Shen – School of Materials Engineering, Purdue University, West Lafayette, Indiana 47907, United States

Dongqi Zheng – School of Electrical and Computer Engineering, Purdue University, West Lafayette, Indiana 47907, United States

Neil R. Dilley – Birck Nanotechnology Center, Purdue University, West Lafayette, Indiana 47906, United States

Raktim Sarma – Sandia National Laboratories, Albuquerque, New Mexico 87185, United States; Center for Integrated Nanotechnologies, Sandia National Laboratories, Albuquerque, New Mexico 87185, United States

Aleem M. Siddiqui – Sandia National Laboratories, Albuquerque, New Mexico 87185, United States

Peide D. Ye – School of Electrical and Computer Engineering, Purdue University, West Lafayette, Indiana 47907, United States;  [orcid.org/0000-0001-8466-9745](https://orcid.org/0000-0001-8466-9745)

Complete contact information is available at:

<https://pubs.acs.org/doi/10.1021/acs.cgd.2c01300>

**Notes**

The authors declare no competing financial interest.

**ACKNOWLEDGMENTS**

This work is supported by the U.S. Office of Naval Research (N00014-20-1-2600). Z.H., H.D., and H.W. acknowledge the support from the U.S. National Science Foundation (DMR-18-9520 and ECCS-1902644) for some of the optical and electrical testing efforts. This work was supported by the Laboratory Directed Research and Development program at Sandia National Laboratories, a multi-mission laboratory managed and operated by National Technology and Engineering Solutions of Sandia, LLC, a wholly owned subsidiary of Honeywell International, Inc., for the U.S. Department of Energy's National Nuclear Security Administration under contract DE-NA-003525. The article describes objective technical results and analysis. Any subjective views or opinions that might be expressed in the article do not necessarily represent the views of the U.S. Department of Energy or the United States Government.

**REFERENCES**

- (1) Dou, H.; Gao, X.; Zhang, D.; Dhole, S.; Qi, Z.; Yang, B.; Hasan, M. N.; Seo, J.-H.; Jia, Q.; Hellenbrand, M.; MacManus-Driscoll, J. L.; Zhang, X.; Wang, H. Electroforming-Free HfO<sub>2</sub>:CeO<sub>2</sub> Vertically Aligned Nanocomposite Memristors with Anisotropic Dielectric Response. *ACS Appl. Electron. Mater.* **2021**, *3*, 5278–5286.
- (2) Si, M.; Murray, A.; Lin, Z.; Andler, J.; Li, J.; Noh, J.; Alajlouni, S.; Niu, C.; Lyu, X.; Zheng, D.; Maize, K.; Shakouri, A.; Datta, S.; Agrawal, R.; Ye, P. D. BEOL Compatible Indium-Tin-Oxide Transistors: Switching of Ultrahigh-Density 2-D Electron Gas Over 0.8 × 10<sup>14</sup> /Cm<sup>2</sup> at Oxide/Oxide Interface by the Change of Ferroelectric Polarization. *IEEE Trans. Electron Devices* **2021**, *68*, 3195–3199.
- (3) Van Toan, N.; Tuoi, T. T. K.; Inomata, N.; Toda, M.; Ono, T. Aluminum Doped Zinc Oxide Deposited by Atomic Layer Deposition and Its Applications to Micro/Nano Devices. *Sci. Rep.* **2021**, *11*, 1204.
- (4) Hill, N. A. First Principles Study of Multiferroic Magnetoelectric Manganites. *AIP Conf. Proc.* **2000**, *535*, 372–382.
- (5) Inomata, A.; Kohn, K. Pyroelectric Effect and Possible Ferroelectric Transition of Helimagnetic GdMn<sub>2</sub>O<sub>5</sub>, TbMn<sub>2</sub>O<sub>5</sub> and YMn<sub>2</sub>O<sub>5</sub>. *J. Phys.: Condens. Matter* **1996**, *8*, 2673.
- (6) Shin, K.-H.; Inoue, M.; Arai, K.-I. Elastically Coupled Magneto-Electric Elements with Highly Magnetostrictive Amorphous Films and PZT Substrates. *Smart Mater. Struct.* **2000**, *9*, 357.
- (7) Srinivas, A.; Suryanarayana, S. v.; Kumar, G. S.; Mahesh Kumar, M. Magnetoelectric Measurements on Bi<sub>5</sub>FeTi<sub>3</sub>O<sub>15</sub> and Bi<sub>6</sub>Fe<sub>2</sub>Ti<sub>3</sub>O<sub>18</sub>. *J. Phys.: Condens. Matter* **1999**, *11*, 3335.
- (8) Yang, F.; Tang, M. H.; Ye, Z.; Zhou, Y. C.; Zheng, X. J.; Tang, J. X.; Zhang, J. J.; He, J. Eight Logic States of Tunneling Magnetoelectroresistance in Multiferroic Tunnel Junctions. *J. Appl. Phys.* **2007**, *102*, 044504.
- (9) Kosub, T.; Kopte, M.; Hühne, R.; Appel, P.; Shields, B.; Maletinsky, P.; Hübner, R.; Liedke, M. O.; Fassbender, J.; Schmidt, O. G.; Makarov, D. Purely Antiferromagnetic Magnetoelectric Random Access Memory. *Nat. Commun.* **2017**, *8*, 13985.
- (10) Bibes, M.; Barthélémy, A. Towards a Magnetoelectric Memory. *Nat. Mater.* **2008**, *7*, 425–426.
- (11) Velev, J. P.; Duan, C.-G.; Burton, J. D.; Smogunov, A.; Niranjan, M. K.; Tosatti, E.; Jaswal, S. S.; Tsymbal, E. Y. Magnetic Tunnel Junctions with Ferroelectric Barriers: Prediction of Four Resistance States from First Principles. *Nano Lett.* **2009**, *9*, 427–432.
- (12) Scott, J. F. Multiferroic Memories. *Nat. Mater.* **2007**, *6*, 256–257.
- (13) Choi, E.-M.; Kleibeuker, J. E.; Fix, T.; Xiong, J.; Kinane, C. J.; Arena, D.; Langridge, S.; Chen, A.; Bi, Z.; Lee, J. H.; Wang, H.; Jia, Q.; Blamire, M. G.; MacManus-Driscoll, J. L. Interface-Coupled BiFeO<sub>3</sub>/BiMnO<sub>3</sub> Superlattices with Magnetic Transition Temperature up to 410 K. *Adv. Mater. Interfac.* **2016**, *3*, 1500597.
- (14) Cheong, S.-W.; Mostovoy, M. Multiferroics: A Magnetic Twist for Ferroelectricity. *Nat. Mater.* **2007**, *6*, 13–20.
- (15) Chen, A.; Bi, Z.; Jia, Q.; MacManus-Driscoll, J. L.; Wang, H. Microstructure, Vertical Strain Control and Tunable Functionalities in Self-Assembled, Vertically Aligned Nanocomposite Thin Films. *Acta Mater.* **2013**, *61*, 2783–2792.
- (16) Azuma, M.; Kanda, H.; Belik, A. A.; Shimakawa, Y.; Takano, M. Magnetic and Structural Properties of BiFe<sub>1-x</sub>Mn<sub>x</sub>O<sub>3</sub>. *J. Magn. Magn. Mater.* **2007**, *310*, 1177–1179.
- (17) Zhu, X. H.; Béa, H.; Bibes, M.; Fusil, S.; Bouzehouane, K.; Jacquet, E.; Barthélémy, A.; Lebeugle, D.; Viret, M.; Colson, D. Thickness-Dependent Structural and Electrical Properties of Multiferroic Mn-Doped BiFeO<sub>3</sub> Thin Films Grown Epitaxially by Pulsed Laser Deposition. *Appl. Phys. Lett.* **2008**, *93*, 082902.
- (18) Pálová, L.; Chandra, P.; Rabe, K. M. Multiferroic BiFeO<sub>3</sub>-BiMnO<sub>3</sub> Nanoscale Checkerboard from First Principles. *Phys. Rev. B* **2010**, *82*, 075432.
- (19) Pálová, L.; Chandra, P.; Rabe, K. M. Magnetostructural Effect in the Multiferroic BiFeO<sub>3</sub>-BiMnO<sub>3</sub> Checkerboard from First Principles. *Phys. Rev. Lett.* **2010**, *104*, 037202.
- (20) Choi, E.-M.; Patnaik, S.; Weal, E.; Sahonta, S.-L.; Wang, H.; Bi, Z.; Xiong, J.; Blamire, M. G.; Jia, Q. X.; MacManus-Driscoll, J. L. Strong Room Temperature Magnetism in Highly Resistive Strained Thin Films of BiFeO<sub>0.5</sub>Mn<sub>0.5</sub>O<sub>3</sub>. *Appl. Phys. Lett.* **2011**, *98*, 012509.
- (21) Choi, E.; Fix, T.; Kursumovic, A.; Kinane, C. J.; Arena, D.; Sahonta, S.; Bi, Z.; Xiong, J.; Yan, L.; Lee, J.; Wang, H.; Langridge, S.; Kim, Y.; Borisevich, A. Y.; MacLaren, I.; Ramasse, Q. M.; Blamire, M. G.; Jia, Q.; MacManus-Driscoll, J. L. Room Temperature Ferrimagnetism and Ferroelectricity in Strained, Thin Films of BiFeO<sub>0.5</sub>Mn<sub>0.5</sub>O<sub>3</sub>. *Adv. Funct. Mater.* **2014**, *24*, 7478–7487.
- (22) Chen, A.; Zhou, H.; Bi, Z.; Zhu, Y.; Luo, Z.; Bayraktaroglu, A.; Phillips, J.; Choi, E.-M.; MacManus-Driscoll, J. L.; Pennycook, S. J.; Narayan, J.; Jia, Q.; Zhang, X.; Wang, H. A New Class of Room-Temperature Multiferroic Thin Films with Bismuth-Based Supercell Structure. *Adv. Mater.* **2013**, *25*, 1028–1032.
- (23) Gim, Y.; Hudson, T.; Fan, Y.; Kwon, C.; Findikoglu, A. T.; Gibbons, B. J.; Park, B. H.; Jia, Q. X. Microstructure and Dielectric Properties of Ba<sub>1-x</sub>Sr<sub>x</sub>TiO<sub>3</sub> Films Grown on LaAlO<sub>3</sub> Substrates. *Appl. Phys. Lett.* **2000**, *77*, 1200–1202.
- (24) Kendall, K. R.; Navas, C.; Thomas, J. K.; zur Loye, H.-C. zur. Recent Developments in Oxide Ion Conductors: Aurivillius Phases. *Chem. Mater.* **1996**, *8*, 642–649.
- (25) Li, L.; Zhang, W.; Khatkhatay, F.; Jian, J.; Fan, M.; Su, Q.; Zhu, Y.; Chen, A.; Lu, P.; Zhang, X.; Wang, H. Strain and Interface Effects in a Novel Bismuth-Based Self-Assembled Supercell Structure. *ACS Appl. Mater. Interfaces* **2015**, *7*, 11631–11636.
- (26) Zhu, Y.; Chen, A.; Zhou, H.; Zhang, W.; Narayan, J.; MacManus-Driscoll, J. L.; Jia, Q.; Wang, H. Research Updates: Epitaxial Strain Relaxation and Associated Interfacial Reconstructions: The Driving Force for Creating New Structures with Integrated Functionality. *APL Mater.* **2013**, *1*, 050702.
- (27) Zhang, W.; Li, M.; Chen, A.; Li, L.; Zhu, Y.; Xia, Z.; Lu, P.; Boullay, P.; Wu, L.; Zhu, Y.; MacManus-Driscoll, J. L.; Jia, Q.; Zhou, H.; Narayan, J.; Zhang, X.; Wang, H. Two-Dimensional Layered Oxide Structures Tailored by Self-Assembled Layer Stacking via Interfacial Strain. *ACS Appl. Mater. Interfaces* **2016**, *8*, 16845–16851.
- (28) Chen, A.; Zhou, H.; Zhu, Y.; Li, L.; Zhang, W.; Narayan, J.; Wang, H.; Jia, Q. Stabilizing New Bismuth Compounds in Thin Film Form. *J. Mater. Res.* **2016**, *31*, 3530–3537.
- (29) Li, L.; Cheng, J.; Wang, H.; Huang, J.; Gao, X.; Wang, X.; Misra, S.; Zhang, B.; Jian, J.; Chen, A.; Lu, P.; Qian, X.; Yang, K.; Wang, H. Interfacial Engineering Enabled Novel Bi-Based Layered Oxide Supercells with Modulated Microstructures and Tunable Physical Properties. *Cryst. Growth Des.* **2019**, *19*, 7088–7095.
- (30) Kalaswad, M.; Zhang, B.; Wang, X.; Wang, H.; Gao, X.; Wang, H. Integration of Highly Anisotropic Multiferroic BaTiO<sub>3</sub>-Fe

- Nanocomposite Thin Films on Si towards Device Applications. *Nanoscale Adv.* **2020**, *2*, 4172–4178.
- (31) Kalaswad, M.; Zhang, D.; Gao, X.; Contreras, L. L.; Wang, H.; Wang, X.; Wang, H. Integration of Hybrid Plasmonic Au–BaTiO<sub>3</sub> Metamaterial on Silicon Substrates. *ACS Appl. Mater. Interfaces* **2019**, *11*, 45199–45206.
- (32) Hyun, S.; Char, K. Effects of Strain on the Dielectric Properties of Tunable Dielectric SrTiO<sub>3</sub> Thin Films. *Appl. Phys. Lett.* **2001**, *79*, 254–256.
- (33) Wong, K. H.; Leung, Y. S. Heteroepitaxial Growth of La<sub>0.7</sub>Ca<sub>0.3</sub>MnO<sub>3</sub>/SrTiO<sub>3</sub>/TiN/Si by Pulsed Laser Deposition. *Thin Solid Films* **1999**, *354*, 55–58.
- (34) Kao, C.-K.; Kuraganti, N. P.; Tsai, C.-H.; Lin, I.-N.; Pandey, R. K.; Ma, K.-J. Preparation of Textured Growth Pb(Zr,Ti)O<sub>3</sub> Thin Films on Si Substrate Using SrTiO<sub>3</sub> as Buffer Layers. *Integrated Ferroelectrics* **2003**, *57*, 1257–1264.
- (35) Kalaswad, M.; Zhang, B.; Wang, H.; Wang, X.; Huang, J.; Wang, H. Tailorable Fe Nanostructures and Magnetic Anisotropy in (La<sub>0.5</sub>Sr<sub>0.5</sub>FeO<sub>3</sub>)<sub>1-x</sub>:Fe<sub>x</sub> Thin Films Integrated on SrTiO<sub>3</sub> and Silicon Substrates. *Mater. Today Adv.* **2020**, *8*, 100112.
- (36) Martinez, A. B.; Godard, N.; Aruchamy, N.; Milesi-Brault, C.; Condurache, O.; Bencan, A.; Glinsek, S.; Granzow, T. Solution-Processed BiFeO<sub>3</sub> Thin Films with Low Leakage Current. *J. Eur. Ceram. Soc.* **2021**, *41*, 6449–6455.
- (37) Mumtaz, F.; Khan, M. H.; Jaffari, G. H. Correlation between the Composition, Phase, Band Structure, Ferroelectric and Leakage Responses of Bi<sub>1</sub>-Ba Fe<sub>1</sub>-TiyO<sub>3</sub> Thin Films. *Thin Solid Films* **2022**, *758*, 139448.
- (38) Yang, C. H.; Hu, G. D.; Wu, W. B.; Wu, H. T.; Yang, F.; Lu, Z. Y.; Wang, L. Reduced Leakage Current, Enhanced Ferroelectric and Dielectric Properties in (Ce,Fe)-Codoped Na<sub>0.5</sub>Bi<sub>0.5</sub>TiO<sub>3</sub> Film. *Appl. Phys. Lett.* **2012**, *100*, 022909.
- (39) Yi, J.; Zhai, Y.; Fan, A.; Gao, Q.; Liu, L. Interface-Layer-Assisted Reliable Ferroelectricity in BiFeO<sub>3</sub> Thin Films by Chemical Solution Deposition. *J. Eur. Ceram. Soc.* **2022**, *42*, 5643–5651.
- (40) Zhao, B.; Yan, Y.; Bi, J.; Xu, G.; Xu, Y.; Yang, X.; Fan, L.; Liu, M. Improved Ferroelectric Properties in Hf<sub>0.5</sub>Zr<sub>0.5</sub>O<sub>2</sub> Thin Films by Microwave Annealing. *Nanomaterials* **2022**, *12*, 3001.
- (41) Faraz, A.; Ricote, J.; Jimenez, R.; Maity, T.; Schmidt, M.; Deepak, N.; Roy, S.; Pemble, M. E.; Keeney, L. Exploring Ferroelectric and Magnetic Properties of Tb-Substituted m = 5 Layered Aurivillius Phase Thin Films. *J. Appl. Phys.* **2018**, *123*, 124101.
- (42) Wang, H.; Li, L.; Huang, J.; Gao, X.; Sun, X.; Zemlyanov, D.; Wang, H. Two-Phase Room-Temperature Multiferroic Nanocomposite with BiMnO<sub>3</sub>-Tilted Nanopillars in the Bi<sub>2</sub>W<sub>1</sub>-XMn<sub>x</sub>O<sub>6</sub> Matrix. *ACS Appl. Mater. Interfaces* **2019**, *11*, 26261–26267.
- (43) Lorenz, M.; Lazenka, V.; Schwinkendorf, P.; Bern, F.; Ziese, M.; Modarresi, H.; Volodin, A.; Van Bael, M. J.; Temst, K.; Vantomme, A.; Grundmann, M. Multiferroic BaTiO<sub>3</sub>–BiFeO<sub>3</sub> Composite Thin Films and Multilayers: Strain Engineering and Magnetoelectric Coupling. *J. Phys. D: Appl. Phys.* **2014**, *47*, 135303.
- (44) Vaz, C. A. F. Electric Field Control of Magnetism in Multiferroic Heterostructures. *J. Phys.: Condens. Matter* **2012**, *24*, 333201.
- (45) Shvets, V. A.; Spesivtsev, E. v.; Rykhllitskii, S. v.; Mikhailov, N. N. Ellipsometry as a High-Precision Technique for Subnanometer-Resolved Monitoring of Thin-Film Structures. *Nanotechnol. Russ.* **2009**, *4*, 201–214.
- (46) Paldi, R. L.; Wang, X.; Sun, X.; He, Z.; Qi, Z.; Zhang, X.; Wang, H. Vertically Aligned Ag<sub>x</sub>Au<sub>1-x</sub> Alloyed Nanopillars Embedded in ZnO as Nanoengineered Low-Loss Hybrid Plasmonic Metamaterials. *Nano Lett.* **2020**, *20*, 3778–3785.
- (47) Paldi, R. L.; Sun, X.; Wang, X.; Zhang, X.; Wang, H. Strain-Driven In-Plane Ordering in Vertically Aligned ZnO–Au Nanocomposites with Highly Correlated Metamaterial Properties. *ACS Omega* **2020**, *5*, 2234–2241.
- (48) Paldi, R. L.; Sun, X.; Phuah, X. L.; Lu, J.; Zhang, X.; Siddiqui, A.; Wang, H. Deposition Pressure-Induced Microstructure Control and Plasmonic Property Tuning in Hybrid ZnO–Ag<sub>x</sub>Au<sub>1-x</sub> Thin Films. *Nanoscale Adv.* **2021**, *3*, 2870–2878.
- (49) De, S.; Muller, F.; Thunder, S.; Abdulazhanov, S.; Laleni, N.; Lederer, M.; Ali, T.; Raffel, Y.; Dunkel, S.; Mojumder, S.; Vardar, A.; Beyer, S.; Seidel, K.; Kampfe, T. 28 Nm HKMG-Based Current Limited FeFET Crossbar-Array for Inference Application. *IEEE Trans. Electron Devices* **2022**, *69*, 7194–7198.
- (50) Misra, S.; Li, L.; Gao, X.; Jian, J.; Qi, Z.; Zemlyanov, D.; Wang, H. Tunable Physical Properties in BiAl<sub>1-x</sub>Mn<sub>x</sub>O<sub>3</sub> Thin Films with Novel Layered Supercell Structures. *Nanoscale Adv.* **2020**, *2*, 315–322.
- (51) Li, L.; Boullay, P.; Lu, P.; Wang, X.; Jian, J.; Huang, J.; Gao, X.; Misra, S.; Zhang, W.; Perez, O.; Steciuk, G.; Chen, A.; Zhang, X.; Wang, H. Novel Layered Supercell Structure from Bi<sub>2</sub>AlMnO<sub>6</sub> for Multifunctionalities. *Nano Lett.* **2017**, *17*, 6575–6582.
- (52) Shen, J.; He, Z.; Zhang, D.; Lu, P.; Deitz, J.; Shang, Z.; Kalaswad, M.; Wang, H.; Xu, X.; Wang, H. Tunable Physical Properties in Bi-Based Layered Supercell Multiferroics Embedded with Au Nanoparticles. *Nanoscale Adv.* **2022**, *4*, 3054–3064.
- (53) Gao, X.; Li, L.; Zhang, D.; Wang, X.; Jian, J.; He, Z.; Wang, H. Novel Layered Bi<sub>3</sub>MoMTO<sub>9</sub> (MT = Mn, Fe, Co and Ni) Thin Films with Tunable Multifunctionalities. *Nanoscale* **2020**, *12*, 5914–5921.
- (54) He, Z.; Gao, X.; Zhang, D.; Lu, P.; Wang, X.; Kalaswad, M.; Rutherford, B. X.; Wang, H. Tailorable Multifunctionalities in Ultrathin 2D Bi-Based Layered Supercell Structures. *Nanoscale* **2021**, *13*, 16672–16679.
- (55) Gradauskaitė, E.; Campanini, M.; Biswas, B.; Schneider, C. W.; Fiebig, M.; Rossell, M. D.; Trassin, M. Robust In-Plane Ferroelectricity in Ultrathin Epitaxial Aurivillius Films. *Adv. Mater. Interfac.* **2020**, *7*, 2000202.

## Recommended by ACS

### Selective Surface Modification and Layer Thinning of MoS<sub>2</sub> via Ultraviolet-Light Irradiation in an Ionic Solution: Implications for Multifunctional Nanoelectronic Devices

Lei Zhang, Dawei Li, et al.

MARCH 27, 2023

ACS APPLIED NANO MATERIALS

READ

### Dominant Two-Dimensional Electron–Phonon Interactions in the Bulk Dirac Semimetal Na<sub>3</sub>Bi

Drhuv C. Desai, Marco Bernardi, et al.

APRIL 24, 2023

NANO LETTERS

READ

### Nonzero Spontaneous Magnetic Moment along the b-Axis and the 2-Fold Spin Reorientation Transition in a Er<sub>0.4</sub>Gd<sub>0.6</sub>FeO<sub>3</sub> Single Crystal

Lingling Wang, Anhua Wu, et al.

MARCH 02, 2023

CRYSTAL GROWTH & DESIGN

READ

### Preparation and Structural Investigation of Ultra-Uniform Mo Films on a Si/SiO<sub>2</sub> Wafer by the Direct-Current Magnetron Sputtering Method

Zhengwang Cheng, Xinguo Ma, et al.

JANUARY 09, 2023

CRYSTAL GROWTH & DESIGN

READ

Get More Suggestions >